Received: 17 May 2022 | Revised: 17 July 2022 | Accepted: 3 August 2022

DOI: 10.1111/jace.18705

Journal of the American Ceramic Society

RESEARCH ARTICLE

Solid-state NMR investigation of fast sodium ion-conducting glass–ceramics: The system $Na_{3+3x-y}RE_{1-x}P_ySi_{3-y}O_9$ (RE = Sc, Y)

Igor d'Anciães Almeida Silva[1] | **Ana Candida M. Rodrigues**[2] | **Hellmut Eckert**[1,3]

[1]Instituto de Física de São Carlos, Universidade de São Paulo, São Carlos, Brazil

[2]Departamento de Engenharia de Materiais, Universidade Federal de São Carlos, São Carlos, Brazil

[3]Institut für Physikalische Chemie, WWU Münster, Münster, Germany

Correspondence
Hellmut Eckert, Instituto de Física de São Carlos, Universidade de São Paulo, São Carlos, Brazil.
Email: eckerth@uni-muenster.de

Funding information
Center for Research, Technology, and Education on Vitreous Materials, Grant/Award Number: 2013/07793-6; FAPESP, Grant/Award Number: 2017/17800-0

Abstract

Glasses and glass–ceramics of composition $Na_{3+3x-y}RE_{1-x}P_ySi_{3-y}O_9$ were synthesized using RE = Sc and Y, $x = 0.4$, and $y = 0.0$ and 0.3 to obtain multiple-phase glass–ceramics containing the highly conducting $Na_5RESi_4O_{12}$ (N5) phase. In addition, the two model compounds $Na_5ScSi_4O_{12}$ and $Na_5InSi_4O_{12}$ were synthesized. Samples were characterized at two distinct annealing stages using X-ray powder diffraction, electrical conductivity measurements, and multinuclear solid-state magic angle spinning (MAS) nuclear magnetic resonance (NMR) spectroscopy. The N5 phase is dominantly formed for Sc-containing glass–ceramics (both with $y = 0.0$ and 0.3) at crystallization temperatures above 900°C. For the other glass–ceramics, the crystallized phases were dominantly $Na_3RESi_2O_7$ (N3), RE = Sc and Y, and $Na_9YSi_6O_{18}$ (N9) phases. ^{29}Si MAS-NMR peak assignments were done with the aid of ^{29}Si{^{45}Sc} rotational echo adiabatic passage double resonance (REAPDOR) experiments. ^{29}Si and ^{23}Na MAS-NMR spectra reveal complex phase compositions and local environment distributions, which could be largely assigned based on known semiempirical chemical shift correlations with average Si–O and Na–O bond distances. ^{31}P MAS and ^{31}P{^{45}Sc} REAPDOR NMR results suggest the presence of orthophosphate groups, arguing against the literature model of isostructural substitution of silicon by phosphorus in the N5 phase.

KEYWORDS
electrolyte, glass–ceramics, nuclear magnetic resonance, structure

1 | INTRODUCTION

The continued interest in sodium-based fast ion conductors stems from their potential use as solid electrolytes in all-solid-state batteries.[1–3] Glass–ceramics produced by controlled crystallization of specific precursor glasses are suitable candidates for such applications.[3,4] Two important systems being explored are based on the Na-super ion conductors (NASICON) and $Na_5YSi_4O_{12}$ (N5) lattices. NASICON glass–ceramics with high Na^+

ionic conductivity are challenging to synthesize because the high amount of sodium needed limits the number of compositions available by the glass–ceramic route.[3] In contrast, glass–ceramics with N5-type structures can be produced more easily by controlled crystallization of sodium silicate glass systems. Moreover, this system offers compositional degrees of freedom, with regard to both, the sodium/rare-earth cationic inventory and the anionic inventory (partial substitution of silicate by phosphate, leading to formulations with the general composition[5]:

$$Na_{3+3x-y}Y_{1-x}P_ySi_{3-y}O_9 \quad (1)$$

The N5 structure comprises 12 silicon oxide tetrahedra arranged in a ring-like structure connected by octahedrally coordinated rare-earth ions. Here, two different sites of Si, both of which are of the Q^2 type (two Si–O–Si linkages), are possible: one connected to two rare-earth octahedra and one connected to only one rare-earth octahedron. The structure is reported to contain both immobile and mobile sodium ions: the immobile ones are found in the interior of the silicate rings, whereas the mobile ones are found outside these rings.[6]

Yamashita et al. reported that the ionic conductivity in this system can be tuned by the replacement of Y^{3+} ions with other trivalent rare-earth ions and/or compositional (x and y) variations concerning the cationic and anionic inventory.[7–9] The authors found that, for $x = 0.4$ and $y = 0.3$, the substitution of Y^{3+} ions by Gd^{3+} ions rendered an ionic conductivity of 0.13 S/cm at 300°C and that the N5-type structure can also be realized for larger rare-earth ions such as Sm^{3+} (ionic radius of 95.8 pm for sixfold coordination[10]). For Nd^{3+} (ionic radius of 98.3 pm for sixfold coordination[10]) and La^{3+} (ionic radius of 103.2 pm[10]), however, the N5 structure was not realized,[9] and other, less-conducting phases, such as $Na_3YSi_3O_9$ (N3) and $Na_9YSi_6O_{18}$ (N9), are formed instead.[5,7,11] Okura et al. established that single-phase highly conductive N5-type structures can be produced if the product $(1 - x)y$ ([Y] × [P]) ranges between 0.12 and 0.2.[12]

These studies employed X-ray diffraction (XRD) powder, impedance spectroscopy, and SEM to probe structure and ion mobility and may lead to results that are difficult to interpret in multiphase samples. Moreover, the previous techniques do not yield information on local structural environments. Element-selective and inherently quantitative structural information on a local level is, in principle, available from solid-state nuclear magnetic resonance (NMR), which has proven immensely useful for the characterization of glasses and glass–ceramics. The only previous application of this technique to the current system is the one by Hung et al. in 2004[13] who measured ^{29}Si magic angle spinning (MAS)-NMR spectra on $Na_5InSi_4O_{12}$ prepared by hydrothermal reaction.

Here we report our NMR results on the structural transformation of $Na_{3+3x-y}RE_{1-x}P_ySi_{3-y}O_9$ (RE = Sc, Y with $x = 0$ and 0.4 and $y = 0$ and 0.3) into glass–ceramics at different annealing stages. XRD and impedance spectroscopy were used to identify the main crystallized phases and to characterize their ionic conductivities. The results from these techniques allow comparison between our samples and literature data. Additionally, we report $^{29}Si\{^{45}Sc\}$ and $^{31}P\{^{45}Sc\}$ rotational echo adiabatic passage double resonance (REAPDOR) experiments on glass–ceramic samples that crystallized the N5 phase to support ^{29}Si NMR peak assignments, spatial proximities in glasses and glass–ceramics, and structural conclusions. Only a few other works relating double resonance studies involving rare-earth nuclei have been published so far on inorganic materials.[14–20]

2 | EXPERIMENTAL PROCEDURES

2.1 | Sample preparation and characterization

Precursor glasses with compositions $Na_{3.9}RE_{0.6}P_{0.3}Si_{2.7}O_9$ (NRPS), $Na_{4.2}RE_{0.6}Si_3O_9$ (NRS), (RE = Sc, Y), and $Na_5ScSi_4O_{12}$ (N5ScS), as well as the reference material $Na_5InSi_4O_{12}$ (N5InS), were produced by mixing stoichiometric ratios of Na_2CO_3 (Vetec, 99%), SiO_2 (Zetasil, >99.9%), $NH_4H_2PO_4$ (Sigma, ≥98%), Sc_2O_3 (ABCR, 99.9%), In_2O_3 (ABCR, 99.9%), and Y_2O_3 (REEtec, 99.9941%). Homogenized powders were heated at 900°C in a platinum crucible for 1 h to decompose the phosphorus precursor ($NH_4H_2PO_4$) and eliminate water and CO_2. NRPS glasses were melted at 1350°C for 1 h, whereas NRS, N5ScS, and N5InS glasses were melted at 1500°C for 3 h.[7,21] All precursor glasses were annealed at 500°C for 3 h to relieve thermal stress. Synthesized glasses were characterized by the DSC (Netzsch DSC 404) analysis with a heating rate of 10°C/min to determine the glass transition (T_g) and crystallization peak (T_p) temperatures (Figure 1 and Table 1). In various cases, two crystallization peaks were identified, indicating two-stage crystallization. Glass–ceramics were produced by the heat treatment of the precursor glasses at approximately (T_g—50) °C during 1 h for nucleation followed by another 1-h treatment at T_p for crystal growth [4, 7]. For glass compositions undergoing two-stage crystallization, separate samples were investigated, following annealing at the two distinct crystallization peak temperatures. Glass–ceramic samples were labeled according to the corresponding annealing temperatures (T_p values):

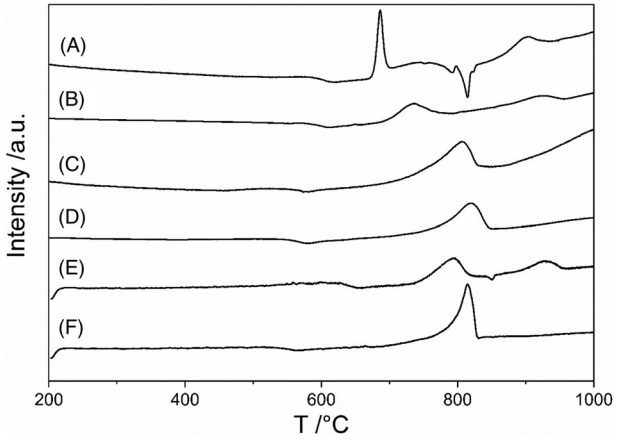

FIGURE 1 DSC thermograms for precursor glasses, as indicated by NScS-G (A), NScPS-G (B), NYS-G (C), NYPS-G (D), N5ScS-G (E), and N5InS-G (F). Values of T_g and T_p are listed in Table 1. Individual thermograms obtained for the different glasses are plotted with a vertical offset.

NScPS-736; NScPS-925; NYPS-820; NScS-690; NScS-905; NYS-806; N5ScS-794; N5ScS-930; and N5InS-815.

XRD powder patterns were measured for both glass and glass–ceramic samples at room temperature in a Rigaku Ultima IV X-ray diffractometer using Cu K_α radiation, diffraction angle values between 10° and 80° in steps of 0.02°, and an integration time of 1 s. Lattice parameters, unit cell volume, and the estimated fractions of crystallized phases were found by Rietveld refinements of the experimental XRD powder patterns by the software MAUD.[22]

Impedance spectroscopy was done in a Novocontrol Alpha Analyzer coupled with a Novotherm furnace. Experiments were conducted at temperatures between 40 and 250°C (accuracy ± 0.1°C), frequencies in the 10^7–0.1-Hz range, and voltage amplitudes of 300 mV. Total ionic conductivity σ was calculated using

$$\sigma = \frac{L}{RA} \tag{2}$$

where L is the sample thickness, and A is the area of the electrode in contact with the sample. R is the total resistance of the sample, acquired from the impedance plots by both WinFIT and EIS Spectrum Analyzer softwares.[23] Activation energies (E_a), ionic conductivities at room temperature and 300°C (σ_{RT} and σ_{300}), and pre-exponential constants (σ_0) were obtained assuming that the temperature dependence of the total ionic conductivity follows an Arrhenius behavior:

$$\sigma\ (T) = \sigma_0 \exp\left(\frac{-E_a}{k_B T}\right) \tag{3}$$

TABLE 1 Glass transition (T_g) and crystallization peak (T_p) temperatures from the DSC thermograms depicted in Figure 1

Sample	T_g (°C)	T_p (°C)
NScS-G	588	686[a]/905[b]
NYS-G	547	806
NScPS-G	580	736[a]/925[b]
NYPS-G	547	820
N5ScS-G	640	794[a]/930[b]
N5InS-G	538	815

Note: The estimated errors are 2°C.
[a]First exothermic peak.
[b]Second exothermic peak.

2.2 | NMR studies

^{31}P and ^{29}Si MAS-NMR spectra were measured in an Agilent DD2 600-MHz spectrometer interfaced with a 5.64-T magnet. Single-pulse ^{31}P (resonance frequency: 98.12 MHz) experiments used a commercial 3.2-mm probe operated at a spinning speed of 8.0 kHz, $\pi/2$ pulses of 3.0μs length, and a relaxation delay of 600 s. Single-pulse ^{29}Si (resonance frequency: 48.16 MHz) experiments were done in a commercial 7.5-mm probe using a spinning speed of 5.0 kHz, $\pi/2$ pulses of 5.5 μs length, and relaxation delays between 900 and 1500 s. Chemical shift values were referenced using powdered BPO_4 (−29.27 ppm against 1-M 85% H_3PO_4 solution) and tetramethylsilane, respectively. All the deconvolution analyses of the experimental NMR spectra were performed using the DMFit software.[24]

^{23}Na and ^{45}Sc MAS NMR experiments were conducted in a Bruker Avance 600 spectrometer with a 14.1-T magnet. Single-pulse ^{23}Na (resonance frequency: 158.76 MHz) and ^{45}Sc (resonance frequency: 145.85 MHz) experiments used a commercial triple-channel 2.5-mm probe, $\pi/6$ pulses of 0.27 and 0.21 μs lengths, respectively, and relaxation delays of 1.0 and 0.1 s, respectively. Chemical shift values were referenced to solid NaCl (7.2 ppm against 1-M aqueous solution of NaCl) and powdered $ScPO_4$ (−48.2 ppm[25] against 1-M solution of $ScCl_3$). ^{23}Na TQMAS experiments at a spinning speed of 20 kHz were performed on all samples containing the N5 crystalline phase using the triple-quantum zero-filter pulse sequence proposed by Amoureux et al.[26] The first two hard pulses were set considering a nutation frequency of 141 kHz and pulse lengths of 3.55 and 1.30 μs, respectively. The third soft pulse for single-quantum coherence detection was a $\pi/2$ pulse with

a length of 18.0 μs. The time increment defining the TQ coherence evolution and thus defining the dwell time in the indirect dimension was 50 μs, and 280 separate t_1 increments were acquired. For each TQ evolution time t_1, 180 scans were acquired using a recycle delay of 0.9 s. The States method[27] was used to separate echo and anti-echo signals, and the 2D dataset was Fourier transformed and sheared according to Massiot et al.[28]

Single-point ^{29}Si{^{45}Sc} REAPDOR experiments were measured on the Bruker Avance Neo system taken on sample NScS-905 using the same probe operated at a spinning speed of 10.0 kHz. Dipolar recoupling between ^{29}Si and ^{45}Sc nuclei was achieved using the pulse sequence of Gullion,[29] where adiabatic mixing is affected by continuous-wave irradiation of the ^{45}Sc nuclei during one third of the rotor period (33 μs). This generates the S signal, which is compared to a reference signal taken without adiabatic mixing (S_0). ^{29}Si π pulses of 6.0 μs were used for ^{29}Si recoupling and rotor-synchronized detection. Various mixing times (1.0, 1.4, and 2.0 ms) were tested. Owing to the long ^{29}Si spin–lattice relaxation times (~1000 s), a pre-saturation pulse train composed of 20 $\pi/2$ pulses of 3.0 μs was used. ^{31}P{^{45}Sc} REAPDOR experiments were conducted in an analogous fashion. In this case, a shorter mixing time (0.6 ms) was used, which was necessary because of the relatively short ^{31}P spin–spin relaxation times limiting the intensity of the S_0 reference signal.

3 | RESULTS AND DISCUSSION

3.1 | X-ray powder diffraction

Figure 2 presents XRD powder patterns for glass samples and crystallized NRS and NPRS samples. For sample NScPS-G, a small amount of a crystalline phase is present. This phase could not be identified, but it does not interfere with the transparency of the sample.

For crystallized NRPS and NRS samples, Rietveld refinements showed that samples NScPS-925 and NScS-905 crystallized in the intended Sc-containing N5 structure. In the latter case, a portion of Na_2SiO_3 (~22%) was also observed. In contrast, samples NScPS-735 and NScS-686, presented the $Na_3ScSi_2O_7$[30] structure (N3) as the main crystallized phase, alongside sodium silicate phases. For R = Y, sample NYPS-820 crystallized in the N9 structure,[31] whereas sample NYS-806 crystallized forming both Y-containing N9 and N3[32] structures but no N5 phase. Finally, stoichiometric N5ScS-930 crystallized in the wanted N5 phase (around 70%) alongside the N3 phase (around 30%), whereas sample N5ScS-794 crystallized N3 (around 65%) alongside δ-$Na_2Si_2O_5$ (around 30%) and a small amount of the N5 phase (around 5%). Table 2 summarizes the lattice parameters and the unit cell volumes found by the Rietveld refinements of the experimental powder patterns for our samples. As one can see, the data presented for samples NScPS-925 and NScS-905 cannot prove the successful substitution of silicon by phosphorus in the tetrahedral framework sites because the lattice parameters were found to be unaltered from those of the P-free $Na_5ScSi_4O_{12}$ as reported by Merinov et al.[6]

3.2 | Ionic conductivity

Impedance spectra were measured for all samples, and representative impedance plots are shown in Figure 3. It was not possible to separate the contribution of grain and grain boundary. Thus, Arrhenius plots for the total conductivity σ are displayed in Figure 4, approximating the prefactor to be temperature independent over the limited temperature range studied here. Values for the activation energies were found by fitting temperature-dependent data with Equation (3) and are shown in Table 3 alongside the values of the logarithm of the pre-exponential term of the Arrhenius expression, $\log(\sigma_0)$, and ionic conductivities at room temperature and 300°C. Typical values of $\log(\sigma_0)$ are expected to be around 2 for ionic conductors.[33] However, lower values have also been found[34] and are attributed to geometrical constraints[35] due to cracks and poor contact between grains,[36] or multiphase systems, as in the present case. Table 3 also shows the values of these parameters reported for $Na_5ScSi_4O_{12}$ crystals[37] and glass–ceramics presenting the N5, N3, and N9 structures.[12,38,39] From the data summarized in this table, one can see that the highest ionic conductivity at 300°C is found for samples NScPS-925 and NScS-905, which crystallize in the N5 structure, with ionic conductivity values of 9.80×10^{-3} and 5.14×10^{-3} S/cm at 300°C, respectively. In the case of NScS-905, there are indications of two distinct activation energies, which might arise from the presence of substantial amounts of crystalline Na_2SiO_3 detected by XRD and solid-state NMR. The conductivities measured for NScPS-925 and NScS-905 are higher than that reported by Okura et al. for $Na_{3.9}Sc_{0.6}P_{0.3}Si_{2.7}O_9$ glass–ceramic,[12] which has the same composition as NScPS-925. In addition, our samples present lower activation energies.

On the other hand, samples NScPS-736 and NScS-686, which crystallized in the N3 structure, presented the lowest ionic conductivity at 300°C among all our samples (1.10×10^{-5} and 5.29×10^{-5} S/cm, respectively), being lower than the ionic conductivity measured for the precursor glasses. This is in agreement with the results of Banks et al.,[38] who compare the ionic conductivity of $Na_{3.2}Y_{0.7}Si_{2.9}P_{0.1}O_9$ glass–ceramic, which crystallized in the N3 structure, with its precursor glass. The values

TABLE 2 Lattice parameters and unit cell volumes found by Rietveld refinements of the experimental X-ray powder patterns and comparison with literature values

Sample	Phase	%	a (Å)	b (Å)	c (Å)	$(V \pm \Delta V)$ (Å^3)
NScS-686	$Na_3ScSi_2O_7$	46.01 ± 0.22	5.362 ± 0.001	9.375 ± 0.002	13.119 ± 0.004	659.50 ± 0.27
	δ-$Na_2Si_2O_5$	33.12 ± 0.22	4.847 ± 0.001	8.226 ± 0.003	12.148 ± 0.004	484.36 ± 0.26
	Na_2SiO_3	20.87 ± 0.22	10.523 ± 0.005	6.057 ± 0.003	4.843 ± 0.001	308.68 ± 0.22
NScPS-736	$Na_3ScSi_2O_7$	65.97 ± 0.41	5.3609 ± 0.0004	9.3615 ± 0.0007	13.141 ± 0.001	659.50 ± 0.09
	δ-$Na_2Si_2O_5$	34.03 ± 0.41	4.8453 ± 0.0004	8.366 ± 0.001	12.085 ± 0.001	489.87 ± 0.08
NScS-905	$Na_5ScSi_4O_{12}$	78.06 ± 0.12	21.688 ± 0.002	21.688 ± 0.002	12.442 ± 0.001	5068.12 ± 1.02
	Na_2SiO_3	21.94 ± 0.12	4.826 ± 0.0006	6.078 ± 0.001	6.087 ± 0.001	178.55 ± 0.05
NScPS-925	$Na_5ScSi_4O_{12}$	100.0 ± 0.00	21.687 ± 0.002	21.687 ± 0.002	12.439 ± 0.002	5066.43 ± 1.24
NYS-806	$Na_9YSi_6O_{18}$	85.16 ± 0.37	15.1314 ± 0.0004	15.1314 ± 0.0004	15.1314 ± 0.0004	3464.47 ± 0.27
	$Na_3YSi_2O_7$	14.84 ± 0.37	9.4251 ± 0.0007	9.4251 ± 0.0007	13.729 ± 0.002	1056.16 ± 0.22
NYPS-820	$Na_9YSi_6O_{18}$	100.0 ± 0.00	15.1286 ± 0.0003	15.1286 ± 0.0003	15.1286 ± 0.0003	3462.55 ± 0.21
N5ScS-794	$Na_3ScSi_2O_7$	65.09 ± 0.18	5.3566 ± 0.0003	9.3596 ± 0.0005	13.1094 ± 0.0007	657.25 ± 0.06
	δ-$Na_2Si_2O_5$	30.13 ± 0.18	4.8453 ± 0.0007	8.353 ± 0.002	12.088 ± 0.002	489.24 ± 0.16
	$Na_5ScSi_4O_{12}$	4.78 ± 0.18	21.562 ± 0.002	21.562 ± 0.002	12.672 ± 0.002	5102.01 ± 1.24
N5ScS-930	$Na_5ScSi_4O_{12}$	71.99 ± 0.30	21.686 ± 0.001	21.686 ± 0.001	12.450 ± 0.001	5070.45 ± 1.24
	$Na_3ScSi_2O_7$	28.01 ± 0.30	5.422 ± 0.002	9.259 ± 0.003	13.200 ± 0.004	662.67 ± 0.38
N5InS-815	$Na_5InSi_4O_{12}$	100.0 ± 0.00	21.722 ± 0.002	21.722 ± 0.002	12.469 ± 0.002	5095.1 ± 1.24
N5[6]	$Na_5ScSi_4O_{12}$	–	21.679	21.679	12.441	5063
N5[13]	$Na_5InSi_4O_{12}$	–	21.716	21.716	21.448	5083.7
N3[30]	$Na_3ScSi_2O_7$	–	5.354	9.347	13.089	665
N9[31]	$Na_{8.48}Y_{1.28}Si_6O_{18}$	–	15.120	15.120	15.120	3457

Note: The phase column shows the crystalline phases used as the starting point for the refinements.

TABLE 3 Values for activation energy (E_a), log(σ_0), room-temperature ionic conductivity (σ_{RT}), and ionic conductivity at 300°C (σ_{300}) found for all studied glasses and glass–ceramics

Sample	E_a (eV)	log(σ_0) (σ_0: S/cm)	σ_{RT} (S/cm)	σ_{300} (S/cm)	Ref.
N5ScS-G	0.564	1.88	2.56×10^{-8}	8.34×10^{-4}	This work
NScS-G	0.550	1.72	2.59×10^{-8}	7.49×10^{-4}	This work
NYS-G	0.551	1.90	4.33×10^{-8}	1.12×10^{-3}	This work
NScPS-G	0.582	1.62	5.65×10^{-8}	9.52×10^{-4}	This work
NYPS-G	0.551	1.90	4.43×10^{-8}	1.12×10^{-3}	This work
N5ScS-794	0.310	−1.20	3.85×10^{-7}	1.17×10^{-4}	This work
NScS-686	0.308	−1.55	1.61×10^{-7}	5.29×10^{-5}	This work
NScPS-736	0.484	−0.69	1.30×10^{-9}	1.10×10^{-5}	This work
N5ScS-930	0.288	−0.01	1.43×10^{-5}	2.98×10^{-3}	This work
NScS-905	0.213	−0.42	1.02×10^{-4}	5.14×10^{-3}	This work
NScPS-925	0.323	0.83	2.30×10^{-5}	9.80×10^{-3}	This work
NYS-806	0.300	−0.69	1.89×10^{-6}	4.72×10^{-4}	This work
NYPS-820	0.610	2.36	1.3×10^{-8}	9.90×10^{-4}	This work
$Na_5ScSi_4O_{12}$	0.79[a]	5.25[b]	6.31×10^{-5}[b]	2.00×10^{-2}	37
$Na_{3.9}Sc_{0.6}P_{0.3}Si_{2.7}O_9$	0.36[a]	0.67[b]	4.86×10^{-6}[b]	3.20×10^{-3}	12
$Na_{3.2}Y_{0.7}P_{0.1}Si_{2.9}O_9$	0.63[a]	1.93[b]	2.82×10^{-9}[b]	2.44×10^{-4}[b]	38
$Na_{4.35}Y_{0.45}P_{0.3}Si_{2.7}O_9$	0.59[a]	1.86[b]	8.97×10^{-9}[b]	4.20×10^{-4}	39

Note: Data shown for crystalline $Na_5ScSi_4O_{12}$ and for $Na_{3.9}Sc_{0.6}P_{0.3}Si_{2.7}O_9$, $Na_{3.2}Y_{0.7}P_{0.1}Si_{2.9}O_9$, and $Na_{4.35}Y_{0.45}P_{0.3}Si_{2.7}O_9$ glass–ceramics were taken from Refs. [12, 37–39].

[a]Converted from kJ/mol to eV.

[b]Literature data.

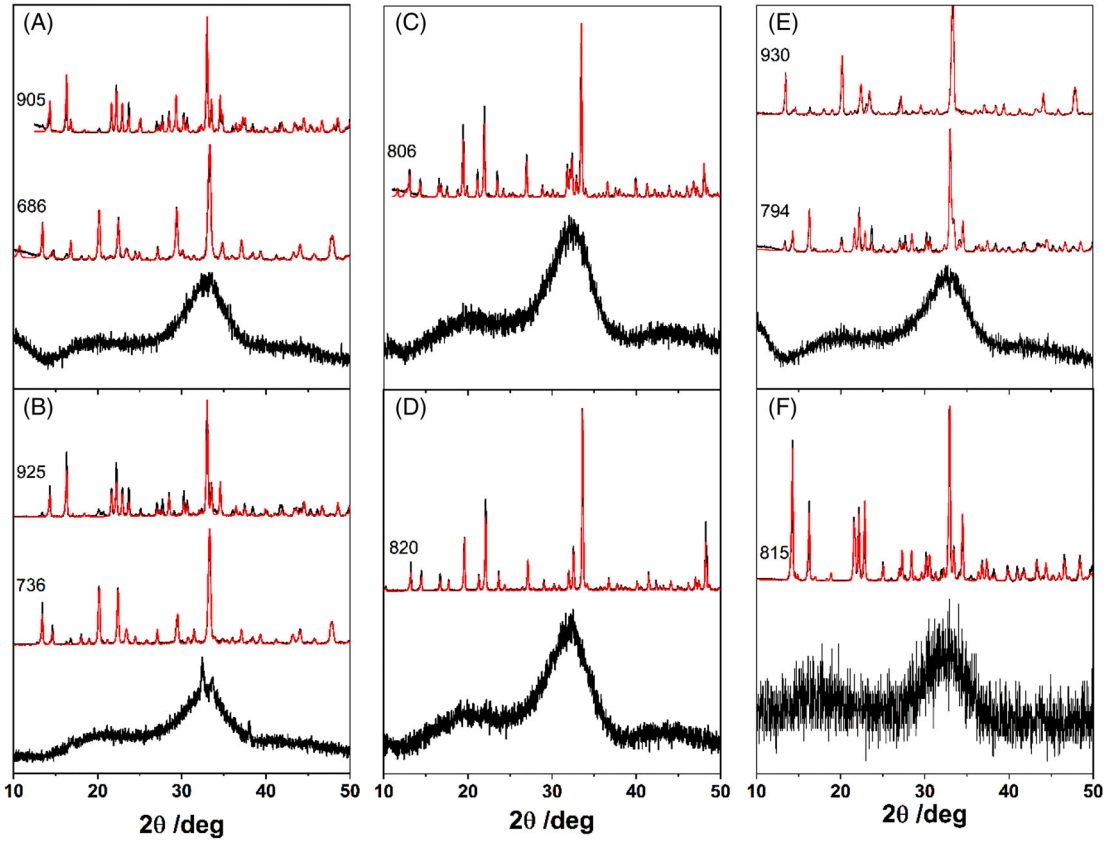

FIGURE 2 X-ray powder patterns (black curves) for glasses and glass–ceramics with compositions $Na_{4.2}Sc_{0.6}Si_3O_9$ (A), $Na_{3.9}Sc_{0.6}P_{0.3}Si_{2.7}O_9$ (B), $Na_{4.2}Y_{0.6}Si_3O_9$ (C), $Na_{3.9}Y_{0.6}P_{0.3}Si_{2.7}O_9$ (D), $Na_5ScSi_4O_{12}$ (E), and $Na_5InSi_4O_{12}$ (F). Numbers indicate the temperature of heat treatment (°C). Red curves represent the Rietveld refinements of the experimental patterns and the lattice parameters found are listed in Table 2. The N5 structure was observed for samples NSS-905 (top pattern at (A)), NSPS-925 (top pattern at (B)), N5ScS-930 (top pattern at (E)), and N5InS-815 (top pattern at (F)).

reported earlier for samples NScPS-736 and NScS-686 are found to be lower than the ionic conductivity at 300°C calculated with the reported parameters from Ref. [38] (2.44×10^{-4} S/cm). This difference may arise from the presence of crystalline sodium silicates alongside the N3 structure in our samples. With exception of the NScPS-736 and NYPS-820 samples, all glass–ceramics display higher ionic conductivity as compared to their precursor glass. Moreover, higher heat-treatment temperatures lead to the crystallization of more conductive phases. NYS-806 has an ionic conductivity comparable with the reported value of 4.20×10^{-4} S/cm at 300°C by Yamashita et al.[39] for $Na_{4.35}Y_{0.45}P_{0.3}Si_{2.7}O_9$ glass–ceramic.

3.3 | ^{29}Si MAS-NMR and ^{29}Si{^{45}Sc} REAPDOR

^{29}Si MAS-NMR spectra of all studied samples are presented in Figure 5, and Table 4 summarizes the deconvolution analyses and assignments. The spectra obtained on the glassy samples are close to identical, indicating very little influence of the type of rare-earth ion present and the partial silicate by phosphate substitution. Consistent with the total network modifier oxide to network former ratio equivalent to 1:1, the results indicate that the structure contains dominantly Q^2 units, but the lineshape asymmetry also suggests Q^3 and Q^1 species. Multiple Q^n sites are typically encountered in the ^{29}Si MAS-NMR spectra of silicate glasses, even if the latter have the stoichiometric composition of a specific Q^n site.[40] Figure 5 indicates a tentative deconvolution, which was constrained to show equal areas for the Q^1 and the Q^3 components, based on the composition of the glass samples. For the glass–ceramic samples NScS-905 and NScPS-925 (top spectrum in Figure 5A,B), two prominent resonances near −85.0 and −79.0 ppm (according to Table 4) were observed and assigned to the two distinct Q^2 sites in the N5 structure. A similar spectrum was observed for isostructural $Na_5InSi_4O_{12}$.[13] However, our spectra do not show the fine splittings observed by Hung et al. for the Si(1) and Si(2) resonances of their hydrothermally prepared N5 samples.[13]

TABLE 4 Chemical shift and full width at half maximum (FWHM) found by numerical deconvolution of the experimental ^{29}Si magic angle spinning (MAS) nuclear magnetic resonance (NMR) spectra

Sample	Area (%)	δ_{iso} (ppm)	FWHM (Hz)	Peak assignment
NScS-G	70.8	−80.0	500	Q^2
	15.4	−88.0	500	Q^3
	13.8	−73.0	500	Q^1
NYS-G	82.2	−80.0	500	Q^2
	10.2	−88.0	500	Q^3
	7.6	−73.0	500	Q^1
NScPS-G	79.5	−81.0	480	Q^2
	10.6	−88.0	480	Q^3
	9.9	−76.8	450	Q^1
NYPS-G	79.5	−81.0	480	Q^2
	10.6	−88.0	480	Q^3
	9.9	−76.8	450	Q^1
N5ScS-G	64.0	−80.2	480	Q^2
	18.0	−90.0	480	Q^3
	18.0	−74.0	450	Q^1
N5InS-G	69.6	−78.3	500	Q^2
	17.4	−88.0	500	Q^3
	13.0	−68.0	520	Q^1
N5ScS-794	44.8	−82.4	85	N3
	19.3	−90.4	85	δ-$Na_2Si_2O_5$
	14.0	−96.8	220	Residual glass
	10.9	−85.0	60	N5 Si(1)
	6.9	−78.8	45	N5 Si(2)
	4.1	−94.5	40	α-$Na_2Si_2O_5$
NScS-686	33.5	−82.3	110	N3
	23.8	−78.8	70	Na_2SiO_3
	20.5	−84.5	120	Residual glass
	8.4	−90.3	110	δ-$Na_2Si_2O_5$
	5.6	−76.8	55	N5 Si(2)
	3.8	−85.3	40	N5 Si(1)
	2.7	−86.2	40	β-$Na_2Si_2O_5$ Si(1)
	1.7	−88.2	40	β-$Na_2Si_2O_5$ Si(2)
NScPS-736	49.4	−88.1	540	Residual glass
	25.6	−82.5	170	N3
	5.6	−79.0	100	N5 Si(2)
	5.4	−90.4	100	δ-$Na_2Si_2O_5$
	5.2	−74.8	210	Residual glass
	3.8	−77.0	90	Na_2SiO_3
	3.2	−85.3	110	N5 Si(1)
	1.4	−94.6	100	α-$Na_2Si_2O_5$
	0.5	−97.7	80	Residual glass
N5ScS-930	40.0	−85.2	40	N5 Si(1)
	32.2	−87.7	320	Residual glass
	28.8	−78.9	40	N5 Si(2)
NScS-905	50.1	−85.2	70	N5 Si(1)
	47.3	−79.1	60	N5 Si(2)
	2.6	−76.8	60	Na_2SiO_3
NScPS-925	50	−79.3	35	N5 Si(2)
	50	−85.4	40	N5 Si(1)
N5InS-815	51.2	−82.9	80	N5 Si(1)
	48.8	−78.2	65	N5 Si(2)

(Continues)

TABLE 4 (Continued)

Sample	Area (%)	δ_{iso} (ppm)	FWHM (Hz)	Peak assignment
NYS-806	64.1	−84.4	180	N9 Si(1) and N3
	26.3	−92.8	130	N9 Si(2)
	6.4	−80.3	40	Residual glass
	3.2	−76.8	40	Na_2SiO_3
NYPS-820	32.0	−84.2	160	N9 Si(1)
	31.0	−87.1	220	β-$Na_2Si_2O_5$
	26.0	−93.2	170	N9 Si(2)
	1.0	−91.2	230	δ-$Na_2Si_2O_5$

Note: Errors were estimated as ±0.2% and ±2% for the areas of the crystalline and glassy components, as ±0.3 and ±1 ppm for δ_{iso} of the crystalline and glassy components and ±5 and ±50 Hz for FWHM for the crystalline and glassy components.

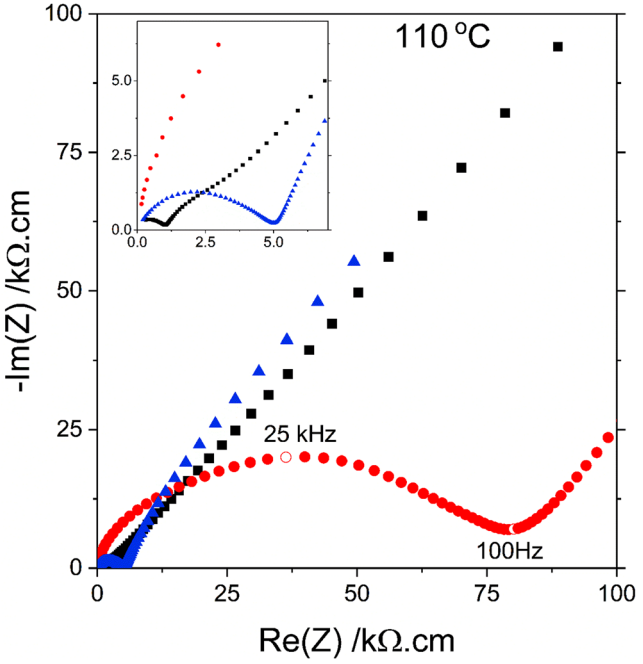

FIGURE 3 Representative impedance plot for glass–ceramics NScS-905 (■), NScS-690 (●), and NYS-806 (▲) at 110°C

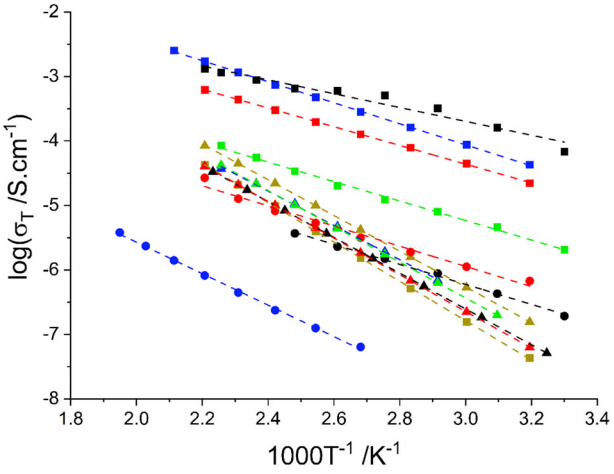

FIGURE 4 Arrhenius plots of the total ionic conductivity for samples NScS-905 (■), NScS-686 (●), NScS-G (▲), NScPS-925 (■), NScPS-736 (●), NScPS-G (▲), N5ScS-930 (■), N5ScS-794 (●), N5ScS-G (▲), NYPS-820 (■), NYPS-G (▲), NYS-806 (■), and NYS-G (▲). Colored dashed lines represent the fitting of the experimental data using Equation (3).

For sample NScS-905, the additional resonance observed at −76.8 ppm (purple line at the top spectrum in Figure 6A) arises from crystalline Na_2SiO_3[41] identified by the XRD results. For the two signals representing the N5 phase, Ref. [13] suggested a tentative peak assignment based on arguments related to Al for Si substitution. Here, a more compelling argument is presented based on the strength of ^{29}Si–^{45}Sc dipole–dipole interactions, which can be predicted by van Vleck theory from internuclear distance distributions.[42] The two silicon sites in N5 differ in the number of Si–Sc next-nearest neighbors (one neighbor for Si(2) and two neighbors for Si(1)). Thus, the van Vleck theory predicts a much larger dipolar second moment $M_{2(Si-Sc)}$ for Si(1) ($M_2 = 5.60 \times 10^6$ rad^2/s^2) than for Si(2) ($M_2 = 3.14 \times 10^6$ rad^2/s^2). To test this prediction, we carried out a single-point ^{29}Si{^{45}Sc} REAPDOR experiment (Figure 6) on sample NScS-905, using a judiciously chosen mixing time of 1.4 ms, for which simulations suggest that these two structural situations will generate sufficiently different REAPDOR attenuations. Indeed, the ratio $(S_0 - S)/S_0$ measured in this experiment is distinctly larger for the resonance around −85.0 ppm compared to that at −79.0 ppm, justifying its assignment to Si(1). Our results agree with the proposed peak assignment given in Ref. [13].

The spectra of NScS-686 and NScPS-736 (middle traces in Figure 5A,B) are more difficult to assign. An estimation of ^{29}Si chemical shifts can be performed using an empirical relationship between the average distance between Si and O atoms in the $Na_3ScSi_3O_7$ crystal structure (d_{Si-O}) and the ^{29}Si chemical shifts[42]:

$$\delta\left(^{29}\mathrm{Si}\right) = 875 \times d_{\mathrm{Si-O}} - 1509 \qquad (4)$$

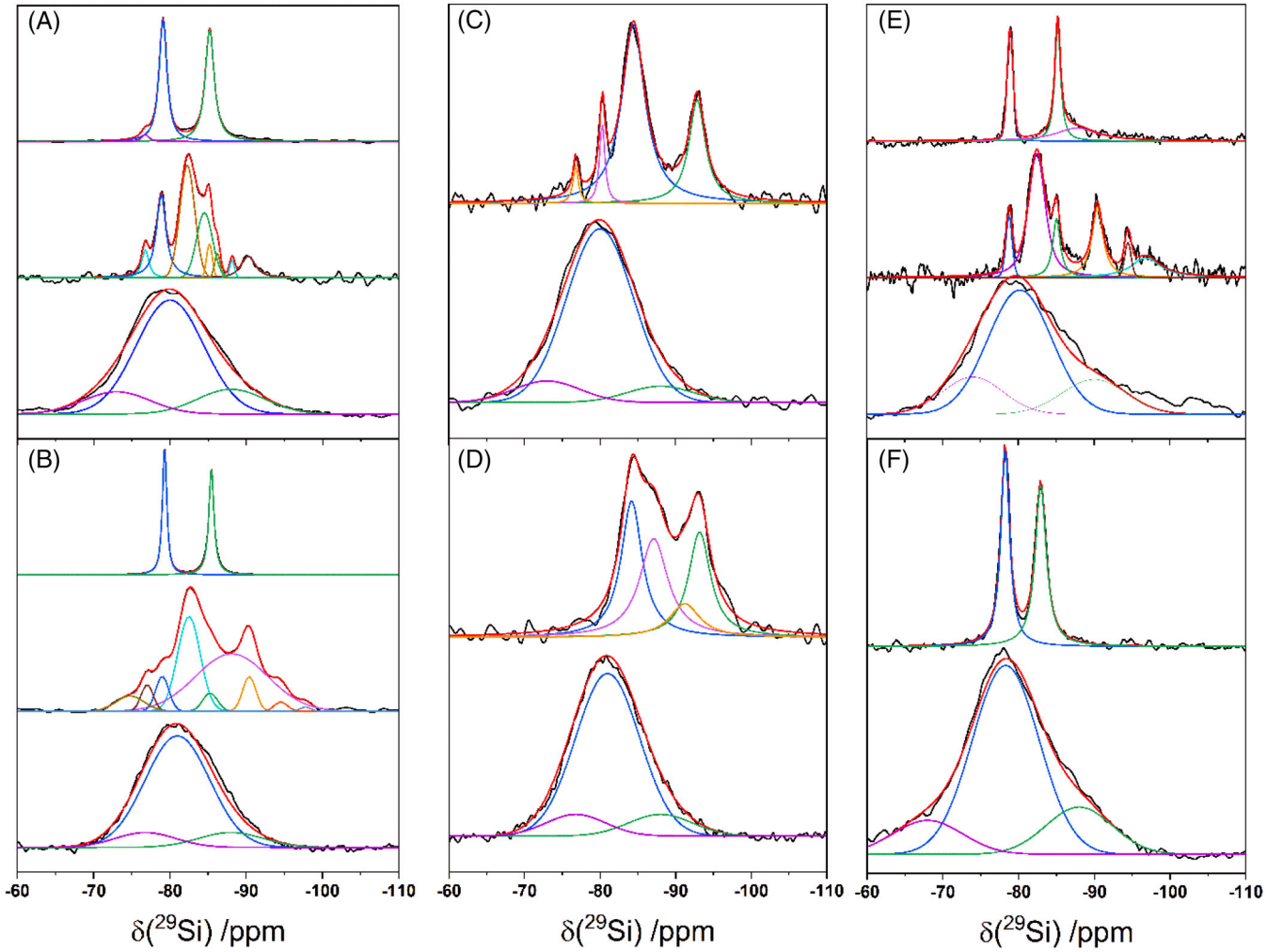

FIGURE 5 ^{29}Si magic angle spinning (MAS) nuclear magnetic resonance (NMR) spectra (black curves) for precursor glass and glass–ceramics of compositions $Na_{4.2}Sc_{0.6}Si_3O_9$ (A), $Na_{3.9}Sc_{0.6}P_{0.3}Si_{2.7}O_9$ (B), $Na_{4.2}Y_{0.6}Si_3O_9$ (C), $Na_{3.9}Y_{0.6}P_{0.3}Si_{2.7}O_9$ (D), $Na_5ScSi_4O_{12}$ (E), and $Na_5InSi_4O_{12}$ (F). Red curves represent numerical deconvolutions of the experimental spectra, and the colored curves represent the individual resonances used to generate the numerical deconvolutions. The dominant presence of the N5 structure is confirmed for samples NScS-905, NScPS-925, N5ScS-930, and N5InS-815 (top spectra at (A, B, E, and F)).

Using the crystallographic data reported by Skehat et al. for the N3 crystal structure,[30] the average distance between Si and O is 1.63066 Å, which leads to a predicted ^{29}Si chemical shift of −82.2 ppm according to Equation (4). Therefore, we assigned the major resonance observed near this value in all three samples heated at the intermediate temperatures (NScPS-736, NScS-686, and N5ScS-794) to silicon nuclei in the $Na_3ScSi_3O_7$ structure, as shown in Table 4. Moreover, the spectra suggest the presence of minor amounts of N5 phase, consistent with the Rietveld data. Regarding the other sharp resonances listed for these samples, they were attributed to Na_2SiO_3, β-, and δ-$Na_2Si_2O_5$,[42] whereas broader signals may be due to residual glassy phase.[43] Although the ^{29}Si NMR chemical shift of −79 ppm also coincides with that of X_2–Sc_2SiO_5,[44] the Rietveld data and the ^{45}Sc MAS-NMR spectra discussed later give no evidence for this phase in our samples.

For the Y-containing glass–ceramics, the ^{29}Si MAS-NMR spectra (top spectra in Figure 5C,D) present two resonances around −84.3 and −93.0 ppm that can be assigned to the two distinct, equally populated silicon sites (expected ratio of 1:1) in the N9 crystal structure. This area ratio is indeed found in the spectrum of sample NYPS-820. For sample NYS-806, these signals are also present, but the area ratio is close to 2:1, at variance with the crystal structure. According to Table 2, NYS-806 also contains a certain amount of the N3 phase (15%), but no distinct resonance could be identified in Figure 5C, middle. Therefore, we conclude that the dominant resonance at −82.2 ppm observed in this sample also contains a contribution from the N3 phase. The remaining ^{29}Si resonances

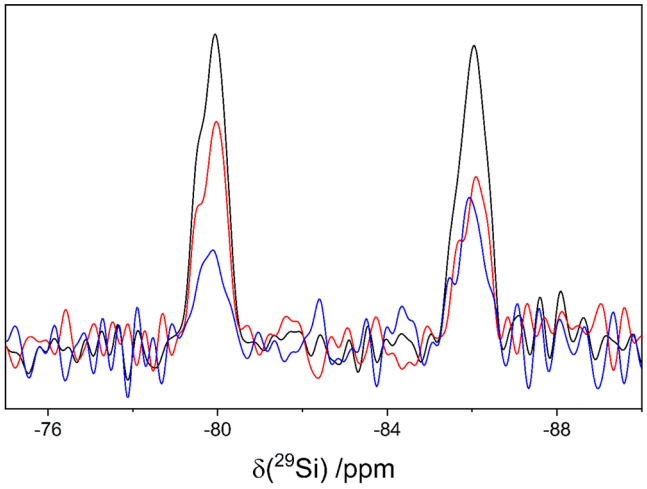

FIGURE 6 $^{29}Si\{^{45}Sc\}$ rotational echo adiabatic passage double resonance (REAPDOR) spectra of sample NScS-905 for a mixing time of 1.4 ms. Black curve represents the S_0 signal, whereas red and blue curves represent the S and $\Delta S = S_0 - S$ signals, respectively. These results show a clear difference in signal dephasing between the resonances at −79.1 and −85.2 ppm and confirm the ^{29}Si magic angle spinning (MAS) nuclear magnetic resonance (NMR) peak assignment (see text).

can be assigned to the various sodium silicate phases that were identified in the Rietveld refinements. Among those, the identification of β-$Na_2Si_2O_5$[41] is based solely on the MAS-NMR data, as the X-ray diffractogram refinements could not identify this particular phase.

3.4 | ^{45}Sc MAS-NMR

Figure 7 summarizes the ^{45}Sc MAS-NMR data. For the precursor glasses N5Sc-G, NScS-G, and NScPS-G a single asymmetrically broadened line centered at an isotropic chemical shift near 77 ppm is observed. The isotropic chemical shifts are consistent with six-coordinated Sc environments, based on the available correlations between ^{45}Sc chemical shifts and possible coordination numbers found in the literature.[15–20,25,45–47] Apart from a small peak at −48.1 ppm, which is attributed to a $ScPO_4$ impurity,[25] there are no significant differences between phosphate-free and phosphate-containing samples. The ^{45}Sc MAS-NMR spectra for the glass–ceramics NScS-905, NScPS-925, and N5ScS-930 are dominated by a narrow resonance with an isotropic chemical shift of 74 ppm, attributed to the expected sixfold coordinated ^{45}Sc nuclei in the $Na_5ScSi_4O_{12}$ crystal structure.[6] For sample NScPS-925, the resonance located around −48 ppm was assigned to crystalline $ScPO_4$.[25] All other resonances listed in Table 5 for the glass–ceramic samples are assigned to scandium in a residual glassy phase. There is no evidence for Sc_2O_3 or scandium silicates[44] in these spectra.

^{45}Sc MAS-NMR data of samples NScS-686, N5ScS-794, and NScPS-736 (middle spectra in Figure 7) displayed several resonances. Parameters found by deconvolution of the experimental spectra (summarized in Table 5) include chemical shift values that can be assigned to sixfold coordinated scandium. As all three glass–ceramics present a resonance around 55 ppm (green curves in Figure 7), this signal is assigned to crystalline $Na_3ScSi_3O_7$ (N3). The presence of several signal components may indicate some structural disorder in the N3 phase, producing multiple scandium environments in their second coordination spheres.

3.5 | ^{23}Na MAS-NMR

Figure 8 summarizes the ^{23}Na MAS-NMR spectra along with their simulations. For the glassy samples, the spectra are very similar, again indicating that neither the type of the rare-earth ion nor the partial substitution of silicon by phosphorus have a profound effect on the sodium environments. Although a deconvolution into two components proved successful, it must be noted that there are many different possibilities of peak deconvolution of these spectra. Even more complex ^{23}Na MAS-NMR spectra are observed for all the Sc-containing glass–ceramics (Figure 8A,B). To develop further constraints for the deconvolution of these NMR spectra, ^{23}Na TQMAS experiments were carried out, but only partial resolution was obtained. Figure 9A shows a representative result; additional spectra are shown in the Supporting Information section. All the TQMAS spectra of the samples predominantly presenting the N5 phase show some lineshape components with moderately weak quadrupolar coupling ($C_Q < 1$ MHz) and up to two components characterized by significantly stronger quadrupolar couplings. Owing to the lower triple-quantum excitation probability for the ^{23}Na nuclei present in the latter, their signal intensities are somewhat under-represented in the TQMAS spectra, whereas the standard MAS-NMR spectra are fully quantitative. The Hamiltonian parameters of the ^{23}Na nuclei identified in the TQMAS spectra can be extracted by fitting the anisotropically broadened lineshapes along the ν_2 dimension at the individual frequencies presenting maxima in the corresponding ν_1 dimension ("slice fitting"). Details are shown in Figures S9–S15 and Table 7. With the Hamiltonian parameters determined in this fashion, and following further parameter refinement, the standard MAS-NMR lineshapes can then be simulated by adjusting the quantitative contributions of each lineshape component through least-squares fitting. In this manner, it was possible to simulate the single-pulse

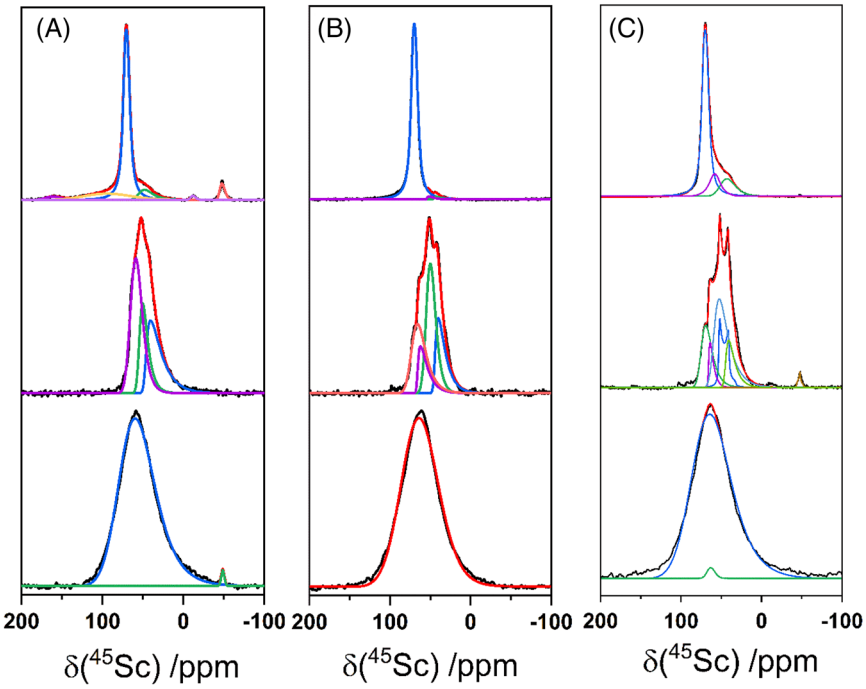

FIGURE 7 ^{45}Sc magic angle spinning (MAS) nuclear magnetic resonance (NMR) spectra (black lines) for glass and glass–ceramics of compositions $Na_{3.9}Sc_{0.6}P_{0.3}Si_{2.7}O_9$ (A), $Na_{4.2}Sc_{0.6}Si_3O_9$ (B), and $Na_5ScSi_4O_{12}$ (C). Red lines represent numerical deconvolutions of the experimental spectra, and the colored lines represent the individual resonances used to generate the numerical deconvolutions. Spectra related to the N5 structure were found for samples NScS-905, NScPS-925, and N5ScS-930 (top spectra at (A), (B), and (C), respectively) where sixfold coordinated Sc was observed. Resonances near −48 ppm are attributed to $ScPO_4$.

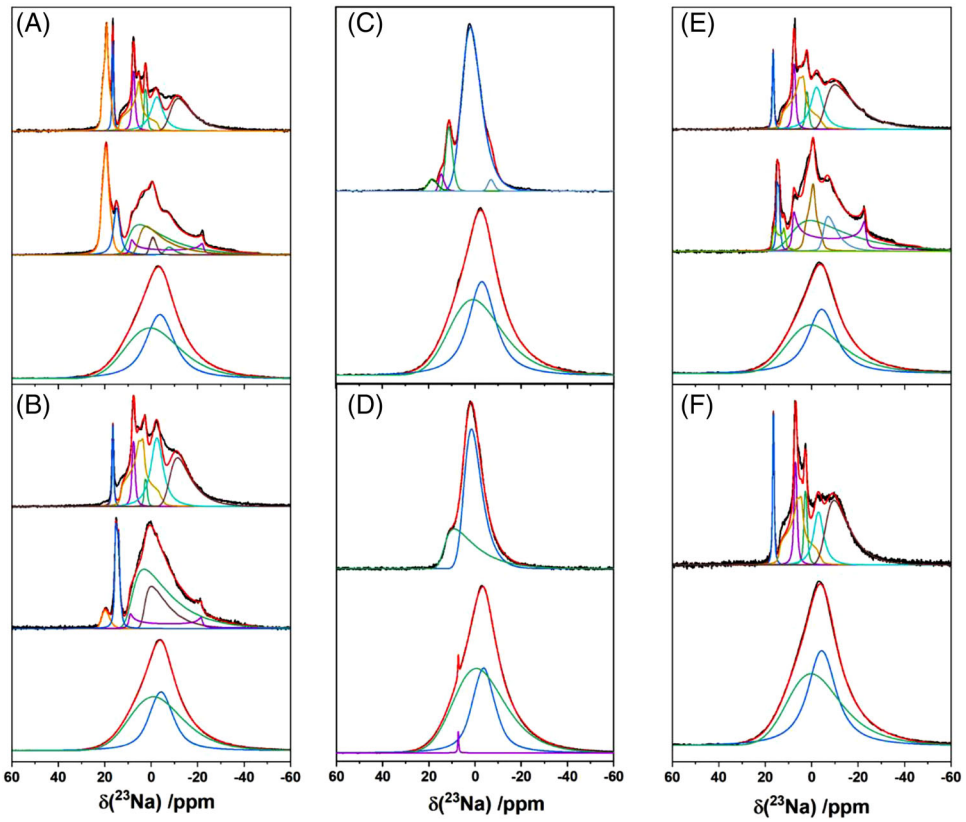

FIGURE 8 ^{23}Na magic angle spinning (MAS) nuclear magnetic resonance (NMR) spectra (black lines) for precursor glass and glass–ceramics of compositions $Na_{4.2}Sc_{0.6}Si_3O_9$ (A), $Na_{3.9}Sc_{0.6}P_{0.3}Si_{2.7}O_9$ (B), $Na_{4.2}Y_{0.6}Si_3O_9$ (C), $Na_{3.9}Y_{0.6}P_{0.3}Si_{2.7}O_9$ (D), $Na_5ScSi_4O_{12}$ (E), and $Na_5InSi_4O_{12}$ (F). Red curves represent simulations of the experimental spectra, and the colored lines represent the individual resonances used to generate the simulations. In the case of the samples presenting dominantly the N5 structure, namely, NScS-905 (top spectrum at (A)), NScPS-925 (top spectrum at (B)), N5ScS-930 (top spectrum at (E)), and N5InS-815 (top spectrum at (F)), the simulations were constrained by the parameters determined via TQMAS. The purple line observed in part (D) of the figure (sample NYPS-G) arises from rotor contamination with NaCl used as a secondary reference.

TABLE 5 ^{45}Sc chemical shifts (δ_{iso}), parameters of the Czjzek model ($\Delta\delta_{iso}$ and $\langle C_Q \rangle$), and quadrupolar Hamiltonian parameters (C_Q and η_Q) considered by modeling the spectra according to second-order perturbation theory, obtained via numerical simulation of the experimental ^{45}Sc magic angle spinning (MAS) nuclear magnetic resonance (NMR) spectra

Sample	Area (%)	δ_{iso} (ppm)	$\Delta\delta_{iso}$ (ppm)	C_Q (MHz)	η_Q
NScS-G	100	78.3	46.7	10.8	–
NScPS-G	99.3	76.8	39.4	12.8	–
	0.7	−48.1	4.5	2.1	–
N5ScS-G	98.7	82.2	46.0	13.7	–
	1.3	66.0	10.0	5.0	–
NScS-686	35.7	54.6	9.9	6.8	–
	29.4	73.4	13.5	9.0	–
	21.9	44.6	4.4	8.7	–
	13.0	66.2	3.0	8.6	–
NScPS-736	45.9	64.5	12.7	7.4	–
	31.6	47.0	5.5	10.7	–
	22.5	54.6	6.6	7.4	–
N5ScS-794	40.8	60.0	10.0	10.0	–
	21.6	75.0	10.0	8.0	–
	16.5	56.0	–	9.0	0.0
	13.1	45.0	5.0	8.0	–
	6.6	66.0	2.0	6.0	–
	1.4	−43.5	–	5.0	1.0
NScS-905	97.3	73.7	–	5.8	0.0
	1.4	54.3	1.9	7.2	–
	1.3	45.5	2.8	6.8	–
NScPS-925	69.2	74.1	–	5.8	0.0
	15.0	113.2	58.1	12.3	–
	7.7	55.3	12.1	9.2	–
	4.4	−45.3	5.4	4.9	–
	2.6	165.0	21.0	5.7	–
	1.1	−10.0	6.2	4.1	–
N5ScS-930	72.2	74.1	–	6.1	0.0
	14.0	50.3	16.0	8.5	–
	13.8	59.8	–	3.8	0.0

Note: Estimated errors are ±1.0% for the areas, ±1.0 ppm for both δ_{iso} and $\Delta\delta_{iso}$, ±0.1 MHz for C_Q, and ±0.05 for η_Q.

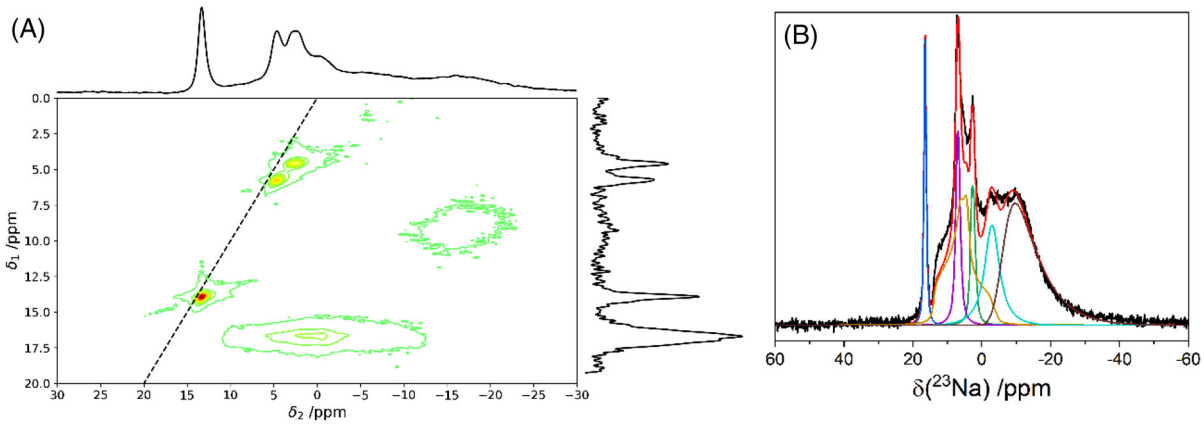

FIGURE 9 ^{23}Na TQMAS spectrum as contour plot (A) and ^{23}Na magic angle spinning (MAS) spectrum (B) of sample N5InS-815. From the TQMAS spectrum, it is possible to differentiate five distinct signals that can be associated with blue, green, purple, dark yellow, and cyan curves at the ^{23}Na MAS deconvolution. Dashed diagonal line at (A) marks the $\delta_1 = \delta_2$ line.

MAS-NMR spectra based on six lineshape components with the final parameters listed in Table 6. A typical example of this fit is shown in Figure 9B.

The next task to be addressed concerns assigning the six ^{23}Na MAS-NMR lineshape components to individual sodium sites in the N5 structure. $Na_5InSi_4O_{12}$ and $Na_5ScSi_4O_{12}$ are isostructural and present six crystallographically inequivalent sodium sites, for the labeling scheme of which we follow reference[17]: Na(5) and Na(6) sites are octahedrally coordinated and found at the center of the silica 12-ring channels in positions (0, 0, 0) and (0, 0, 0.25), respectively; they are considered immobile based on short and regular Na–O bond lengths and nearly isotropic thermal vibrations. Na(3) and Na(4) are located within silica-seven-ring channels and are highly mobile, as indicated by partial occupancy and large anisotropic thermal parameters. Na(1) sites are tetrahedrally coordinated (albeit listed with two additional Na–O distances near 2.9 Å in Ref. [17]) and form connections between the 12-ring and the 7-ring channels; their isotropic thermal parameters suggest them to be immobile. Na(2) sites are distorted octahedral sites (listed as being five-coordinate in Ref. [17]) that form connections between two seven-ring channels; their degree of mobility is uncertain. Considering the Wyckoff multiplicities and partial occupancies, the approximate population ratio is 40:20:13:13:7:7 for Na(1):Na(2):Na(3):Na(4):Na(5):Na(6) in both $Na_5InSi_4O_{12}$[17] and $Na_5ScSi_4O_{12}$.[6] The minor difference noted between Refs. [6] and [17] concerns the nature of Wyckoff site of Na(4), which is, however, without consequence for the intensity distribution of the six Na sites, which is the same between both studies. Guided by the site population ratios, we propose the site assignments listed in Table 6, which also compares the respective fractional contributions as expected from the published site multiplicities and occupancies with the experimentally observed ones. The site assignments are also found to be consistent in that only sites Na(1) and Na(2) display significant electric quadrupole coupling strengths, whereas quadrupolar coupling is weak (as expected) for the octahedral sites Na(5) and Na(6) and for the mobile sites Na(3) and Na(4), where partial averaging of the electric field gradients by sodium ionic motion is expected.

For further support of these assignments, the semiempirical bond valence concept developed by Koller et al.[48] to estimate the ^{23}Na chemical shift is helpful. Koller et al. consider the total bond valence W_i of each sodium–oxygen bond given by

$$W_i = \sum_j s_{ij} = \sum_j \exp\left\{\left(r_0 - r_{ij}\right)/B\right\}$$

where r_0 is the empirical length of an oxygen–cation bond with unit valence, r_{ij} is the oxygen–cation bond length from the crystal structure, and $B = 0.37$ Angstrom is a constant. Values of r_0 for different oxygen–cation bonds are tabulated in Ref. [49]. The ^{23}Na chemical shift (relative to aqueous NaCl solution) is determined by

$$\frac{\delta_{iso}}{ppm} = -133.6\ A + 114.8 \quad (5)$$

where A is given by

$$A = \sum W_i / r_i^3 \quad (6)$$

and r_i is the length of the sodium–oxygen bond, of the sodium ion whose bond valence is being calculated. Note that the offset value in Equation (5) has been increased by 7.2 ppm (relative to the one given by Koller) to a value of 114.8 ppm taking into account aqueous NaCl solution as a reference (Koller used solid NaCl).

It must be borne in mind, however, that a meaningful Koller analysis is only possible for those Na sites that are coordinated to oxygen atoms, the coordination spheres of which are defined by cation sites having full site occupancy. In the absence of full occupancy, local site distortions (changes in bond distances and angles) are expected due to local atomic rearrangements driven by the tendency of local energy minimization. In the N5 structure, only the sodium sites Na(5) and Na(6) satisfy the previous criterion; thus, this type of evaluation is limited to these two sodium sites. Table 8 summarizes the predicted and experimentally determined ^{23}Na MAS-NMR chemical shifts for all the crystalline structures of interest: $Na_5ScSi_4O_{12}$, $Na_5InSi_4O_{12}$, $Na_3ScSi_2O_7$, $Na_3YSi_2O_7$, and $Na_9YSi_6O_{18}$ and the various binary sodium silicates known. For the binary sodium silicate, a tendency of Equation (5) to underestimate the chemical shifts by about 5–7 ppm can be noticed but can be considered to lie within the general scatter of the full dataset of ionic sodium compounds analyzed in Ref. [48]. On the other hand, Equation (5) predicts the chemical shifts of the Na(5) and Na(6) sites rather well in all of the four materials dominantly presenting the N5 structure. The assignment of the sites Na(5) and Na(6) based on Equation (5) is also in good agreement with the quantitative signal area ratios. A similar exercise was done for the Na sites in the N3 phase in those samples in which they are dominant. Various additional broad resonances were observed in some of the ^{23}Na MAS-NMR spectra belonging to residual glassy material and various crystalline sodium silicate phases that were observed from both XRD and ^{29}Si MAS-NMR. As the ^{23}Na MAS-NMR spectra of the glasses and the N3 and N9 phases are rather difficult to analyze because of the poor overall spectroscopic resolution observed in these samples, the following discussion will focus on the spectra

TABLE 6 ^{23}Na chemical shifts (δ_{iso}), parameters of the Czjzek model ($\Delta\delta_{iso}$ and C_Q), and parameters of the model assuming only second-order effects of the quadrupolar interaction in the Zeeman states (C_Q and η_Q) found by deconvolution of the experimental ^{23}Na magic angle spinning (MAS) nuclear magnetic resonance (NMR) spectra for the precursor glasses and the NScS-905 and NScPS-925 glass–ceramics

Sample	Area (%)	δ_{iso} (ppm)	$\Delta\delta_{iso}$ (ppm)	C_Q (MHz)	η_Q	Peak assignment
NScS-G	56.1	9.8	20.0	3.3	–	
	43.9	1.2	-	1.9	1.00	
NYS-G	57.0	9.9	19.3	3.2	–	
	43.0	1.2	–	1.8	1.00	
NScPS-G	63.1	8.0	19.7	3.1	–	
	36.9	1.1	–	2.1	0.8	
NYPS-G	65.8	8.1	19.1	3.2	–	
	33.8	2.0	–	2.1	1.0	
	0.4	7.3	–	–	–	
N5ScS-G	54.7	9.6	19.7	3.6	–	
	45.3	−0.8	–	2.8	1.0	
N5InS-G	54.7	9.6	19.8	3.6	–	
	45.3	−0.8	–	2.0	1.0	
NScS-686	31.6	10.5	3.4	3.6	–	N3 Na(2) + δ-$Na_2Si_2O_5$ Na(2)
	21.7	21.9	–	1.5	0.7	Na_2SiO_3
	20.1	6.0	3.1	3.2	–	Residual glass
	11.8	18.0	–	5.1	0.0	N3 Na(1)
	9.9	16.0	–	1.1	0.0	δ-$Na_2Si_2O_5$ Na(1)
	2.9	0.15	2.6	1.0	–	
	2.0	−6.0	3.0	1.5	–	
NScPS-736	52.5	9.0	5.4	3.5	–	N3 Na(2) + δ-$Na_2Si_2O_5$ Na(2)
	22.4	3.3	2.8	2.8	–	Residual glass
	12.0	16.0	–	1.2	0.1	δ-$Na_2Si_2O_5$ Na(1)
	9.9	18.5	–	5.1	0.0	N3 Na(1)
	3.2	21.0	3.0	1.2	–	Na_2SiO_3
N5ScS-794	38.6	10.0	10.0	4.2	–	N3 Na(2)
	25.4	17.2	–	5.1	0.0	N3 Na(1) +
	13.9	3.2	–	1.7	0.9	Residual glass
	11.2	−5.0	2.5	2.0	–	N5 Na(5)
	5.7	15.4	–	1.0	0.0	δ-$Na_2Si_2O_5$ Na(1)
	5.1	18.0	–	2.0	0.2	?
NScS-905	24.4 (32)	−7.8	4.9	2.6	–	N5 Na(1)
	21.6 (16)	13.5	–	2.4	1.0	N5 Na(2)
	19.7	21.5	–	1.3	1.0	Na_2SiO_3
	16.3 (10)	−1.3	–	1.1	0.0	N5 Na(3)/Na(4)
	7.4 (10)	8.3	–	0.8	0.0	N5 Na(3)/Na(4)
	5.8 (6)	16.8	–	0.6	0.0	N5 Na(6)
	4.8 (6)	3.2	–	0.9	0.3	N5 Na(5)
NScPS-925	31.2 (20)	13.1	–	2.6	0.8	N5 Na(2)
	28.8 (40)	−7.6	4.9	2.5	–	N5 Na(1)
	26.7 (13)	−1.3	–	1.1	0.0	N5 Na(3)/Na(4)
	6.5 (13)	8.3	–	0.8	0.0	N5 Na(3)/Na(4)
	4.2 (7)	16.8	–	0.6	0.0	N5 Na(6)
	2.6 (7)	3.2	–	0.9	0.3	N5 Na(5)
N5ScS-930	39.7 (40)	−5.3	4.9	3.1	–	N5 Na(1)
	26.7 (20)	13.1	–	2.6	0.8	N5 Na(2)
	17.8 (13)	−1.0	–	1.1	0.0	N5 Na(3)/Na(4)
	7.1 (13)	8.2	–	0.8	0.0	N5 Na(3)/Na(4)
	4.5 (7)	16.9	–	0.6	0.0	N5 Na(6)
	4.2 (7)	2.8	–	0.9	0.4	N5 Na(5)

(Continues)

TABLE 6 (Continued)

Sample	Area (%)	δ_{iso} (ppm)	$\Delta\delta_{iso}$ (ppm)	C_Q (MHz)	η_Q	Peak assignment
N5InS-815	36.5 (40)	−5.5	5.7	2.6	–	N5 Na(1)
	27.0 (20)	14.0	–	2.6	0.8	N5 Na(2)
	14.5 (13)	−2.0	–	1.0	0.0	N5 Na(3)/Na(4)
	8.8 (13)	7.6	–	0.8	0.0	N5 Na(3)/Na(4)
	6.7 (7)	16.7	–	0.6	0.0	N5 Na(6)
	6.5 (7)	3.5	–	0.9	0.4	N5 Na(5)
NYS-806	81.8	5.3	7.0	2.0	–	
	11.1	12.3	2.9	1.0	–	
	2.9	19.9	4.0	1.2	–	
	2.3	15.5	1.9	1.0	–	
	1.9	−5.9	2.7	1.0	–	
NYPS-820	66.1	4.7	5.6	2.0	–	
	33.9	14.1	4.6	3.2	–	

Note: Estimated errors are ±1.0% for the areas, ±0.3 ppm for both δ_{iso} and $\Delta\delta_{iso}$, ±0.1 MHz for C_Q, and ±0.05 for η_Q. In column 2, the values in parentheses denote the predicted areas based on the populations and site occupancy data in the stoichiometric compound $Na_5ScSi_4O_{12}$.

TABLE 7 Isotropic chemical shift (δ_{iso}) and second-order quadrupolar effect (SOQE) found by the analysis of the ^{23}Na TQMAS spectra of glass–ceramics containing the N5 phase as the dominant crystalline structure

Sample	δ_{iso} (ppm)	*SOQE* (MHz)
N5InS-815	13.7	0.6
	5.4	0.8
	3.9	1.1
	10.7	3.2
	−0.5	4.0
N5ScS-930	13.7	0.7
	5.2	0.9
	10.2	3.4
NScPS-925	13.8	0.6
	5.2	0.8
	10.2	3.4
NScS-905	13.7	0.6
	5.1	0.9
	11.3	3.0
	10.1	3.4

Note: Estimated errors were ±1.0 ppm for δ_{iso} and ±0.5 MHz for SOQE.

of the phases presenting predominantly the N5 phase, which is the one of greatest interest in this field.

Overall, the comparison of the ^{23}Na MAS-NMR spectra indicates that the sodium site population ratios in the stoichiometric compounds $Na_5InSi_4O_{12}$ and $Na_5ScSi_4O_{12}$ are rather similar; however, the Na(1):Na(2) site population tends to be smaller than 2:1 and approaches the value of 1:1 in the nonstoichiometric compounds, so that the possibility of reversing the Na(1) versus Na(2) site assignments must be considered. Unfortunately the Koller model is not helpful in this respect as both Na(1) and Na(2) are bound to O atoms linked to partially vacant Na sites so that an this question cannot be ultimately resolved. An interesting structure/property correlation indeed emerges when considering the fraction of the sodium ions in the mobile sites Na(3) and Na(4): Sample NScPS-925, the composition of which is nonstoichiometric and has a partial substitution of silicate by phosphate, possesses the highest ionic conductivity of all the samples measured in this study. The ^{23}Na MAS-NMR analysis also reveals that it has an enhanced concentration of the mobile Na(3) and Na(4) sites of 33% compared to 24%–25% of the total sodium inventory in all the other N5-based ceramics, in particular, when compared to stoichiometric $Na_5ScSi_4O_{12}$. Aside from this detail, the results indicate the utility of TQMAS-NMR along with semiempirical methods to approach the analysis and assignment of complex MAS-NMR spectra observed in multiphase glass–ceramic materials.

3.6 | ^{31}P MAS-NMR and ^{31}P{^{45}Sc} REAPDOR

Figure 10 summarizes the ^{31}P MAS-NMR data obtained from the P-containing glasses and glass–ceramics and the results from their analyses are summarized in Table 9. In the glassy state, three lineshape components are observed for both the Sc- and Y-containing samples. All of them are characterized by very small chemical shift anisotropies (no spinning sidebands). Based on this absence and the positive isotropic chemical shifts their most likely assignment is to orthophosphate, P^0 units found in three slightly different local cationic environments. This assignment is consistent with the general observation that phosphorus tends to act as a network modifying ion scavenger in mixed network former glasses, attracting locally more network modifier compared to the overall network modifier to

TABLE 8 Estimated values of ^{23}Na chemical shifts (δ_e) and A parameter using Equations (5) and (6) according to the crystal structures of interest

Crystal structure	Na site	Occupancy	Wyckoff position	A	δ_e (ppm)	Experimental assignment δ_{iso} (ppm)
$Na_5InSi_4O_{12}$	Na(1)	1.0	36f			−5.5
	Na(6)	1.0	6b	0.75	14.8	16.7
	Na(5)	1.0	6a	0.83	4.3	3.5
	Na(2)	1.0	18e			14.0
	Na(3)	1/3	36f			−2.0
	Na(4)	2/3	18d			7.6
$Na_5ScSi_4O_{12}$	Na(1)	1.0	36f			13.1
	Na(6)	1.0	6b	0.69	15.0	16.9
	Na(5)	1.0	6a	0.76	6.5	2.8
	Na(2)	1.0	18e			−5.3
	Na(3)	1/3	36f			−1.0
	Na(4)	1/3	36f			8.2
$Na_3ScSi_2O_7$	Na(1)	1.0	4c	0.67	18.2	18.0
	Na(2)	1.0	8d	0.71	17.0	10.0
Na_2SiO_3	Na(1)	1.0	8b	0.749[a]	14.7	21.5
α-$Na_2Si_2O_5$	Na(1)	1.0	4e	0.730[a]	17.3	24.6
β-$Na_2Si_2O_5$	Na(1)	1.0	4e	0.684[a]	23.4	27.6
	Na(2)	1.0	4e	0.801[a]	7.8	15.5
δ-$Na_2Si_2O_5$	Na(1)	1.0	4e	0.68	24.5	16.0
	Na(2)	1.0	4e	0.78	10.0	10.0

Note: We assumed an error of ±0.1 for A and an error of ±4.1 ppm for the estimated chemical shifts (according to Ref. [48]). Occupancy and Wyckoff multiplicities are also listed. Experimental chemical shifts from sodium silicates were taken from Ref. [48] and re-referenced to aqueous NaCl solution, by adding a fixed value of 7.2 ppm.

[a]Data taken from Ref. [48].

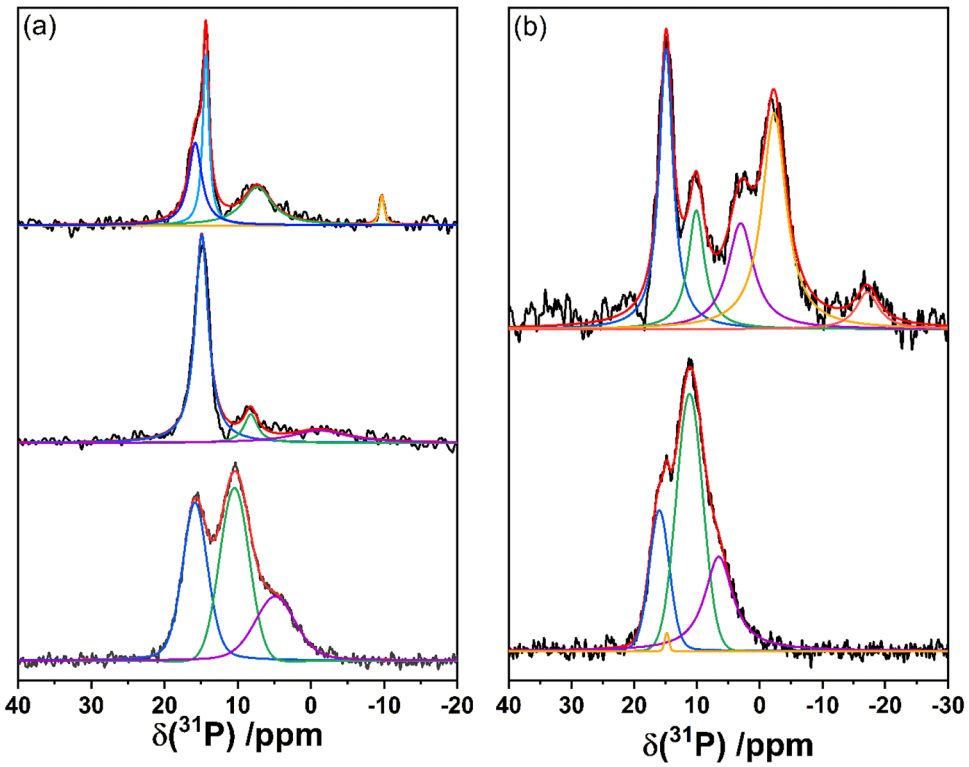

FIGURE 10 ^{31}P magic angle spinning (MAS) nuclear magnetic resonance (NMR) spectra (black curves) of glasses (bottom) and glass–ceramics (A) compositions $Na_{3.9}Sc_{0.6}P_{0.3}Si_{2.7}O_9$: NScPS-736 (middle) and NScPS-925 (top); (B) $Na_{3.9}Y_{0.6}P_{0.3}Si_{2.7}O_9$: NYPS-820. Colored curves represent individual resonances used to generate the numerical deconvolutions (red curves).

TABLE 9 ^{31}P chemical shifts and full width at half maximum (FWHM) values found by deconvolution of the ^{31}P magic angle spinning (MAS) nuclear magnetic resonance (NMR) spectra

Sample	Area (%)	δ_{iso} (ppm)	FWHM (Hz)	Assigt.
NScPS-G	40.5	10.4	460	P^0_{1Sc}
(MAS)	35.8	15.8	400	P^0_{0Sc}
	23.7	4.9	640	P^0_{2Sc}
NScPS-G (REAPDOR— S_0)	47.8	9.9	1140	P^0_{1Sc}
	33.2	16.4	820	P^0_{0Sc}
	19.0	2.9	1850	P^0_{2Sc}
NScPS-G (REAPDOR— S)	46.9	9.9	1140	P^0_{1Sc}
	40.1	16.4	820	P^0_{0Sc}
	12.9	2.9	1850	P^0_{2Sc}
NYPS-G	49.2	11.2	490	P^0_{1Y}
	28.6	6.5	530	P^0_{2Y}
	21.6	16.0	370	P^0_{0Y}
	0.6	14.8	80	P^0(cr)
NScPS-736	71.6	14.9	215	P^0_{0Sc}(g)
	18.3	−1.2	915	P^1(g)
	10.1	8.2	220	P^0_{1Sc}(g)
NScPS-925	32.9	7.3	470	P^0(g)
	31.9	15.8	215	P^0_{0Sc}(cr)
	31.1	14.3	100	P^0_{0Sc}(cr)
	4.1	−9.7	80	$ScPO_4$(cr)
NYPS-820	35.5	−2.3	455	P^1(g)
	26.7	14.9	260	P^0(g)
	18.9	3.0	490	P^1(g)
	13.2	10.1	310	P^0(g)
	5.7	−17.2	425	P^2(g)

Note: Estimated errors: ±1.0% for the areas, ±0.3 ppm for δ_{iso}, and ±20 Hz for FWHM.
Abbreviation: REAPDOR, rotational echo adiabatic passage double resonance.

network former ratio defined by the glass composition. The effect is particularly well known in many bioactive silicate glasses containing low phosphate concentrations.[50] Figure 11, middle, shows ^{31}P{^{45}Sc} REAPDOR results, indicating that the signal attenuation effected by ^{45}Sc dipolar recoupling is virtually absent for the high-frequency component at 15.8 ppm but increases with decreasing ^{31}P chemical shift. This result suggests that the three signal components reflect phosphate units with different numbers of Sc^{3+} ions (presumably zero, one, and two) in their second coordination sphere; an analogous interpretation is suggested for the Y-containing glass.

In analogy to the situation in the glassy state, the ^{31}P MAS-NMR spectrum of the glass–ceramic sample NScPS-925 (top spectrum in Figure 10A) shows two dominant orthophosphate units located at 15.8 and 14.3 ppm (see Table 9) rather than the metaphosphate P^2 units expected in case of substitution of silicate by phosphate within the metasilicate ring structure. These conclusions are confirmed by the results of a single-point ^{31}P{^{45}Sc} REAPDOR measurements shown in Figure 11A. In this case, the REAPDOR result, conducted at a mixing time of 1.4 ms, clearly shows the complete absence of ^{31}P–^{45}Sc dipolar interactions. Evidently, these nuclei are too far apart for a dipolar interaction to be measured on this timescale, suggesting that phosphate does not enter the crystalline N5 phase at all. To summarize, the positive isotropic chemical shifts, the lack of a chemical shift anisotropy and the absence of detectable ^{31}P–^{45}Sc dipolar coupling are clear evidences against the model of an isotypical substitution of Q^2 metasilicate units by analogous metaphosphate (P^2) units within the chains or rings of the N5 host compound. Rather these species must be assigned to orthophosphate groups, which are likely situated in a different phase or in defect sites with mobility averaging out dipole–dipole interactions with the ^{45}Sc nuclei. We further attribute the broad resonance at 11.2 ppm to phosphorus in a residual glassy phase, whereas the narrow resonance at −9.7 ppm arises from $ScPO_4$,[45–47] which is also detected in the ^{45}Sc MAS-NMR spectrum. Likewise, in the spectrum of NScPS-736, the broad resonance at 14.9 ppm indicates that phosphate remains in the glassy phase. There is also no evidence of phosphate entering the $Na_3ScSi_3O_7$ (N3) structure (Figure 10A, middle). Likewise, Figure 10B, top, suggests that in the glass–ceramic NYPS-820, phosphate remains in the glassy part of the ceramic. In this case, the ^{31}P

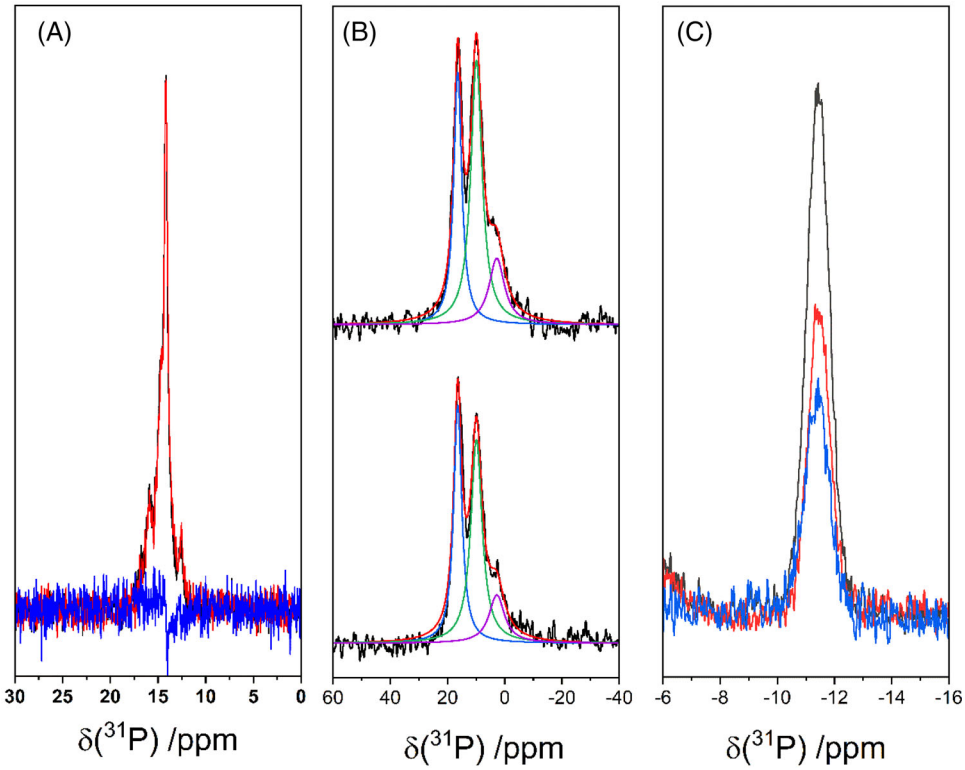

FIGURE 11 $^{31}P\{^{45}Sc\}$ rotational echo adiabatic passage double resonance (REAPDOR) spectra of (A) sample NScPS-925 for a mixing time of 1.4 ms, (B) for sample NSPS-G for a mixing time of 0.6 ms, and (C) for an $ScPO_4$ sample with a mixing time of 0.1 ms. At (A) and (C), black, red, and blue curves indicate S_0, S, and $\Delta S = S_0 - S$ signals, respectively. At (B), the black curves represent experimental S_0 (top) and S (bottom) signals, whereas the red curves represent their numerical deconvolution, and the blue, green, and purple lines represent the individual components of the deconvolutions. These results show that the ^{31}P nuclei in the glassy phase show interactions with ^{45}Sc nuclei of different strengths, whereas in the ceramic phase, the orthophosphate units present in the crystalline state do not interact with the ^{45}Sc nuclei from the N5 phase.

chemical shifts indicate the formation of ortho-, pyro-, and metaphosphate, that is, P^0, P^1, and P^2 units, respectively. Again, there is no evidence of phosphate units entering the N3 or N9 phases.

4 | CONCLUSIONS

$Na_{3+3x-y}RE_{1-x}P_ySi_{3-x}O_9$ glass–ceramics were synthesized using RE = Sc and Y, $x = 0.4$, and $y = 0.0$ and 0.3. Glass–ceramic formation was monitored ex situ by XRD, impedance spectroscopy, and multinuclear solid-state NMR. The desired highly conducting $Na_5RESi_4O_{12}$ (N5) phase is only formed in the Sc-containing samples crystallized above 900°C, whereas heat treatment at lower temperatures results in the dominant formation of the much less conductive N3 phase. The phase distribution observed in the glass–ceramic samples was confirmed by ^{29}Si and ^{23}Na MAS-NMR, the latter of which was able to differentiate between the different sodium sites in the various crystalline phases present. ^{31}P MAS-NMR and $^{31}P\{^{45}Sc\}$ REAPDOR results indicate that the postulated aliovalent substitution of $(SiO_3)^{2-}$ units by $(PO_3)^-$ units in the silicate rings of the N5 structure does not occur; there is also no evidence for phosphate substitution in the N3 and N9 phases. Rather, orthophosphate groups are formed, which either remain in the glassy part of the glass–ceramic, form separate phases, such as $ScPO_4$, or enter vacancy sites in the N5 structure with some mobility averaging ^{31}P–^{45}Sc dipolar interactions. The rather complex ^{23}Na MAS-NMR data could be analyzed successfully based on an analysis of site population ratios and aided by a correlation of ^{23}Na chemical shifts and bond valences of the oxygen atoms to which they are coordinated. Indeed, nonstoichiometric $Na_{3.9}Sc_{0.6}P_{0.3}Si_{2.7}O_9$ has an enhanced population of the mobile Na(3) and Na(4) sites compared to stoichiometric $Na_5ScSi_4O_{12}$, providing a rationale for the higher ionic conductivity measured in $Na_{3.9}Sc_{0.6}P_{0.3}Si_{2.7}O_9$. The results of the present study illustrate the power and potential of solid-state NMR techniques for the structural elucidation of the complex glass–ceramics formed in this system. Finally, the NMR data presented here also provide an idea of the structural organization of the glassy precursors. The data indicate

very little differences between the scandium- and the yttrium-based glasses. Consistent with the network modifier-to-network former ratio of 1:1, the ^{29}Si chemical shifts indicate a dominance of Q^2 units, with Q^1 and Q^3 also being present. Rare-earth ions are dominantly six-coordinated, whereas the phosphate ions are of the Q^0 type, presenting three distinct environments with different numbers of rare-earth ions in their second coordination spheres.

ACKNOWLEDGMENTS

The authors acknowledge the financial support from CeRTEV (Center for Research, Technology, and Education on Vitreous Materials, FAPESP 2013/07793-6). IDA Silva acknowledges the financial support from FAPESP Grant no. 2017/17800-0. We thank Dr. Laís Dantas Silva for assistance with some of the XRD experiments, Dr. Adriana M. Nieto-Muñoz, and Me. Vinícius Zallocco for assistance with the impedance experiments, and Me. Thiago A. Lodi for assistance with some of the heat treatments.

Open access funding enabled and organized by Projekt DEAL.

ORCID

Ana Candida M. Rodrigues https://orcid.org/0000-0003-1689-796X
Hellmut Eckert https://orcid.org/0000-0002-6536-0117

REFERENCES

1. Guin M, Tietz F. Survey of the transport properties of sodium superionic conductor materials for use in sodium batteries. J Power Sources. 2015;271:1056–64.
2. Zhao C, Liu L, Qi X, Lu Y, Wu F, Zhao J, et al. Solid-state sodium batteries. Adv Energy Mater. 2018;8:1703012.
3. Eckert H, Rodrigues ACM. Ion-conducting glass-ceramics for energy-storage applications. MRS Bull. 2017;42:206–12.
4. Okura T. Development of Na^+ superionic conducting $Na_5YSi_4O_{12}$-type glass-ceramics. Adv Mater Lett. 2019;10:85–90.
5. Yamashita K, Nojuri T, Umegaki T, Kanazawa T. New fast sodium-ion conducting glass-ceramics of silicophosphates: crystallization, microstructure and conduction properties. Solid State Ionics. 1989;35:299–306.
6. Merinov BV, Maksimov BA, Belov NV. Crystal structure of Na-scandium silicate, $Na_5ScSi_4O_{12}$. Dokl Akad Nauk SSSR. 1980;255:577–82.
7. Yamashita K, Nojuri T, Umegaki T, Kanazawa T. Na^+ superionic conductors of glass-ceramics in the system Na_2O-Re_2O_3-P_2O_5-SiO_2 (Re = rare earth elements). Solid State Ionics. 1990;40/41:48–52.
8. Yamashita K, Tanaka M, Kakuta T, Matsuda M, Umegaki T. Effects of rare earth elements on the crystallization of the glass-ceramic Na^+ superionic conductor Narpsio-V. J Alloys Compd. 1993;193:283–5.
9. Yamashita K, Umegaki T, Tanaka M, Kakuta T, Nojuri T. Microstructural effects on conduction properties of $Na_5YSi_4O_{12}$-type glass-ceramic Na^+-fast ionic conductors. J Electroceram Soc. 1996;143:2180–6.
10. Shannon RD. Revised effective ionic radii and systematic studies of interatomic distances in halides and chalcogenides. Acta Crystallogr, A 1976;32:751–67.
11. Cervantes Lee F, Marr J, Glasser FP. Compounds in the Na_2O-Y_2O_3-SiO_2 system. Ceram Int. 1981;7:43–7.
12. Okura T, Monma H, Yamashita K. Na^+-fast ionic conducting glass-ceramics of silico-phosphates. J Electroceram. 2010;24:83–90.
13. Hung L-I, Wang S-L, Szu S-P, Hsieh C-Y, Kao H-M, Lii K-H. Hydrothermal synthesis, crystal structure, solid-state NMR, and ionic conductivity of $Na_5InSi_4O_{12}$, a silicate containing a single 12-membered ring. Chem Mater. 2004;16:1660–6.
14. Sebastian CP, Zhang L, Eckert H, Pöttgen R. Structural investigation of ScAuSi and ScAuGe using ^{45}Sc solid state NMR. Z Naturforsch. 2007;62b:173–6.
15. Jaworsky A, Charpentier T, Stevensson B, Edén M. Scandium and yttrium environments in aluminosilicate glasses unveiled by ^{45}Sc/^{89}Y NMR spectroscopy and DFT calculations: what structural factors dictate the chemical shift? J Phys Chem C. 2017;121:18815–29.
16. Mohr D, de Camargo ASS, de Araujo CC, Eckert H. Local environment of scandium in aluminophosphate laser glasses: structural studies by solid state NMR spectroscopy. J Mater Chem. 2007;17:3733–3738.
17. de OliveiraJr M, Uesbeck T, Gonçalves TS, Magon CJ, Pizani PS, de Camargo ASS, Eckert H. Network structure and rare-earth ion local environments in fluoride phosphate photonic glasses studied by solid state NMR and EPR spectroscopies. J Phys Chem C. 2015;119:24574–87.
18. de OliveiraJr M, Gonçalves TS, Ferrari C, Magon CJ, Pizani PS, de Camargo ASS, et al. Structure-property relations in fluorophosphate glasses: an integrated spectroscopic strategy. J Phys Chem C. 2017;121:2968–86.
19. Galleani G, Santagneli SH, Ledemi Y, Messaddeq Y, Janka O, Pöttgen R, et al. Ultraviolet upconversion luminescence in a highly transparent triply-doped Gd^{3+}-Tm^{3+}-Yb^{3+} fluoride-phosphate glasses. J Phys Chem C. 2018;122:2275–84.
20. Galleani G, Doerenkamp C, Santagneli S, Magon CJ, de Camargo ASS, Eckert H. Compositional optimization of emission properties for rare-earth doped fluoride phosphate glasses: structural investigations via NMR, EPR, and optical spectroscopies. J Phys Chem C. 2019;123:31219–31.
21. Nechaev GV, Vlasova SG, Reznitskikh OG. Conductivity in sodium-yttrium-silicate and sodium-yttrium-phosphate glasses. Glass Phys Chem. 2015;41:64–7.
22. Lutterolli L, Bortolotti M, Ischia G, Lonardelli I, Wenk HR. Rietveld texture analysis from diffraction images. Z Krystallogr Suppl. 2007;26:125–30.
23. Bondarenko AS, Ragoisha GA. In: Pomerantsev AL, editor. Progress in chemometrics research. New York: Nova Science Publishers; 2005. p. 89–102.
24. Massiot D, Fayon F, Capron M, King I, Le Calvé S, Alonso B, et al. Modeling one- and two-dimensional solid-state NMR spectra. Magn Reson Chem. 2002;40:70–6.

25. Kim N, Hsieh CH, Stebbins JF. Scandium coordination in solid oxides and stabilized zirconia: ^{45}Sc NMR. Chem Mater. 2006;18:3855–9.
26. Amoureux JP, Fernandez C, Steuernagel S. Z filtering in MQMAS NMR. J Magn Reson, Ser A. 1996;123:116–8.
27. Ernst RR, Bodenhausen G, Wokaun A. Principles of nuclear magnetic resonance in one and two dimensions. Oxford: Clarendon; 1987.
28. Massiot D, Touzo B, Trumeau D, Coutures JP, Virlet J, Florian P, et al. Two-dimensional magic angle spinning isotropic reconstruction sequences for quadrupolar nuclei. Solid State Nucl Magn Reson. 1996;6:73–83.
29. Gullion T. Measurement of dipolar interactions between spin-1/2 and quadrupolar nuclei by rotational-echo, adiabatic passage, double resonance NMR. Chem Phys Lett. 1995;246:325–30.
30. Skehat SM, Simonov VI, Belov NV. The crystal structure of synthetic Na, Sc-silicate, $Na_3Sc[Si_2O_7]$. Dokl Akad Nauk SSSR. 1969;184:337–40.
31. Többens DM, Kalenberg V, Kaindl R, Sartory B, Konzett J. $Na_{8.25}Y_{1.25}Si_6O_{18}$ and its family of *zwölfer* ring silicates. Z Kristallogr. 2008;223:389–98.
32. Merinov BV, Maximov BA, Belov NV. Crystal structure of sodium yttrium silicate $Na_3YSi_2O_7$. Dokl Akad Nauk SSSR. 1981;260:1128–30.
33. Ortiz-Mosquera JF, Nieto-Muñoz AM, Rodrigues ACM. Influence of Al^{3+} on glass forming ability, structural and electrical properties of the $Na_{3.4}Sc_2Si_{0.4}P_{2.6}O_{12}$ superionic conductor. J Alloys Compd. 2021;850:156670.
34. Nieto-Muñoz AM, Ortiz-Mosquera JF, Rodrigues ACM. The role of Al^{3+} on the microstructural and electrical properties of $Na_{1+x}Al_xTi_{2-x}(PO_4)_3$ NASICON glass-ceramics. J Alloys Compd. 2020;820:153148.
35. Mariappan CR, Yada C, Rosciano F, Roling B. Correlation between micro-structural properties and ionic conductivity of $Li_{1.5}Al_{0.5}Ge_{1.5}(PO_4)_3$ ceramics. J Power Sources. 2011;196:6456–64.
36. Nuernberg RB, Rodrigues ACM. A new NASICON lithium ion-conducting glass-ceramic of the $Li_{1+x}Cr_x(Ge_yTi_{1-y})_{2-x}(PO_4)_3$ system. Solid State Ionics. 2017;301:1–9.
37. Shannon RD, Taylor BE, Gier TE, Chen H-Y, Berzins T. Ionic conductivity in $Na_5YSi_4O_{12}$-type silicates. Inorg Chem. 1978;17:958–64.
38. Banks E, Kim CH. Ionic conductivity in glass and glass-ceramics of the $Na_3YSi_3O_9$ and $Na_5YSi_4O_{12}$ type materials. J Electrochem Soc. 1985;132:2617–21
39. Yamashita K, Ohkura S, Umegaki T, Kanazawa T. Synthesis, polymorphs, and sodium ionic conductivity of sodium yttrium silicophosphates with the composition $Na_{3+3x-y}Y_{1-x}P_ySi_{3-y}O_9$. J Ceram Soc Jpn. 1988;96:967–72.
40. Eckert H. Structural characterization of amorphous solids and glasses using solid state NMR. Prog Nucl Magn Reson Spectrosc. 1992;23:159–293.
41. Xue X, Stebbins JF. ^{23}Na NMR chemical shifts and local Na coordination environments in silicate crystals, melts, and glasses. Phys Chem Miner. 1993;20:297–307.
42. MacKenzie KJD, Smith ME. Multinuclear solid-state NMR of inorganic materials. Oxford, UK: Pergamon; 2002.
43. Murdoch JB, Stebbins JF, Carmichael ISE. High-resolution ^{29}Si NMR study of silicate and aluminosilicate glasses: the effect of network-modifying cations. Am Mineral. 1985;70:332–43.
44. Alba MD, Chain P, González-Carrascosa T. Synthesis, Rietveld analysis, and solid state nuclear magnetic resonance of X_2-Sc_2SiO_5. J Am Ceram Soc. 2009;92:487–90.
45. Alba MD, Chain P, Florian P, Massiot D. ^{45}Sc spectroscopy of solids: interpretation of quadrupolar interactions and chemical shifts. J Phys Chem C. 2010;114:12125–32.
46. Bräuniger T, Hoffman AJ, Moudrakovski IL, Hoch C, Schnick W. A ^{45}Sc-NMR and DFT calculation study of crystalline scandium compounds. Solid State Sci. 2016;51:1–7.
47. Mohr D. Solid state NMR studies of scandium compounds. PhD Thesis. WWU Münster; 2010.
48. Koller H, Engelhardt G, Kentgens APM, Sauer J. ^{23}Na NMR spectroscopy of solids: interpretation of quadrupole interaction and chemical shifts. J Phys Chem. 1994;98:1544–51.
49. Brown ID, Altermatt D. Bond-valence parameters obtained from a systematic analysis of the inorganic crystal structure database. Acta Crystallogr, B. 1985;41:244–7.
50. Eckert H. Structural characterization of bioactive glasses using solid state NMR, J Sol-Gel Sci Technol. 2018;88:263–95.

SUPPORTING INFORMATION

Additional supporting information can be found online in the Supporting Information section at the end of this article.

How to cite this article: d'Anciães Almeida Silva I, Rodrigues ACM, Eckert H. Solid-state NMR investigation of fast sodium ion-conducting glass–ceramics: The system $Na_{3+3x-y}RE_{1-x}P_ySi_{3-y}O_9$ (RE = Sc, Y). J Am Ceram Soc. 2022;105:7502–7521.
https://doi.org/10.1111/jace.18705